Force spectroscopy reveals membrane fluctuations and surface adhesion of extracellular nanovesicles impact their elastic behavior

PNAS RESEARCH ARTICLE | BIOPHYSICS AND COMPUTATIONAL BIOLOGY OPEN ACCESS

Force spectroscopy reveals membrane fluctuations and surface adhesion of extracellular nanovesicles impact their elastic behavior

Fredrik Stridfeldt[a,1], Vikash Pandey[b,1], Hanna Kylhammar[a], Moein Talebian Gevari[c], Prattakorn Metem[d], Vipin Agrawal[b,e,f], André Görgens[g,h,i], Doste R. Mamand[g,j,k], Jennifer Gilbert[l], Lukas Palmgren[l], Margaret N. Holme[l], Oskar Gustafsson[g,h], Samir El Andaloussi[g,h], Dhrubaditya Mitra[b,2], and Apurba Dev[a,c,2]

Affiliations are included on p. 10.

Edited by Catherine Murphy, University of Illinois at Urbana-Champaign, Urbana, IL; received July 15, 2024; accepted March 7, 2025

The elastic properties of nanoscale extracellular vesicles (EVs) are believed to influence their cellular interactions, thus having a profound implication in intercellular communication. However, accurate quantification of their elastic modulus is challenging due to their nanoscale dimensions and their fluid-like lipid bilayer. We show that the previous attempts to develop atomic force microscopy-based protocol are flawed as they lack theoretical underpinning as well as ignore important contributions arising from the surface adhesion forces and membrane fluctuations. We develop a protocol comprising a theoretical framework, experimental technique, and statistical approach to accurately quantify the bending and elastic modulus of EVs. The method reveals that membrane fluctuations play a dominant role even for a single EV. The method is then applied to EVs derived from human embryonic kidney cells and their genetically engineered classes altering the tetraspanin expression. The data show a large spread; the area modulus is in the range of 4 to 19 mN/m and the bending modulus is in the range of 15 to 33 $k_B T$, respectively. Surprisingly, data for a single EV, revealed by repeated measurements, also show a spread that is attributed to their compositionally heterogeneous fluid membrane and thermal effects. Our protocol uncovers the influence of membrane protein alterations on the elastic modulus of EVs.

extracellular vesicles | atomic force microscopy | force spectroscopy | elasticity | lipid bilayer

Significance

The purpose of this study is to better understand extracellular vesicles and their nanomechanical properties. This is vital as elasticity is believed to influence cellular interaction and by extension how intercellular communication works. Our results reveal that vesicles have an intrinsic spread in elasticity, which we attribute to thermal fluctuations and compositional heterogeneity. In addition, we develop a framework complete with a theoretical model, experimental technique, and statistical approach to account for this.

The discovery of EVs and their numerous roles in pathophysiological processes are redefining our approaches and understanding of human health and diseases (1, 2). Released to the extracellular milieu by most cell types, these nanovesicles carry a wide variety of cellular components including proteins, nucleic acids, and lipids, and are known to deliver their bioactive cargo to a recipient cell, thereby, inducing functional alterations (3). During the past decade, this topic has generated exploding interest, consequently driving countless technical innovations. While these efforts have helped to overcome many of the initial challenges and skepticism, the high heterogeneity of EVs even when they are released by a single cell has triggered the obvious questions; are there EV subpopulations in circulation that are functionally differential or more relevant than others? If so, which property is the best indicator of such functional differences? While a single EV approach is arguably the best way to address such heterogeneity, given their nanoscale dimension and diverse molecular repertoire, existing techniques can not perform a comprehensive chemical analysis at a single vesicle level. Thus far, optical/fluorescence techniques have been the main methods to interrogate single EVs, although providing only a limited set of information (4, 5). In this context, the recent attempts made with atomic force microscopy (AFM) have brought renewed enthusiasm as it can provide complementary information, e.g., stiffness, bending modulus, and adhesion (6). Given that the stiffness of EVs may influence their cellular uptake, the topic also has larger implications concerning EV biology and functions (7).

Accurate quantification of the stiffness modulus of EVs from force spectroscopy is, however, nontrivial due to the fluidic nature of the membrane and compositional inhomogeneity. Thus far, only a single attempt has been made to develop a protocol (8). Developed on the foundation of the Canham-Helfrich model (CH model), the protocol relies on the assumption that the osmotic pressure difference induced by volume shrinkage plays a dominant role in their stiffness. The migration of water molecules through the lipid bilayer being much slower than a typical timescale of a nanoindentation experiment,

Author contributions: D.M. and A.D. designed research; F.S., V.P., H.K., M.T.G., P.M., V.A., A.G., O.G., D.M., and A.D. performed research; A.G., D.R.M., J.G., L.P., O.G., S.E.A., D.M., and A.D. contributed new reagents/analytic tools; F.S., V.P., H.K., M.T.G., P.M., V.A., A.G., D.M., and A.D. analyzed data; A.D. acquired funding; and F.S., V.P., M.N.H., D.M., and A.D. wrote the paper.

The authors declare no competing interest.

This article is a PNAS Direct Submission.

[1]F.S. and V.P. contributed equally to this work.

[2]To whom correspondence may be addressed. Email: dhrubaditya.mitra@su.se or apurba.dev@angstrom.uu.se.

This article contains supporting information online at https://www.pnas.org/lookup/suppl/doi:10.1073/pnas.2414174122/-/DCSupplemental.

Published April 18, 2025.

the validity of such an assumption needs careful reevaluation. The protocol also fails to convincingly address two fundamental aspects, namely: i) the competition between adhesion and shape deformation leading to a different mechanism of tether formation for surface adhered vesicles (9, 10), which is the case for most EV studies with AFM and ii) the effect of membrane fluctuations on the elastic property (11). To what extent these effects influence the elastic modulus of EVs remains unknown and so is the accuracy of all the previous reports (12, 13). Besides, it is also unknown if the alteration in the membrane protein composition can induce measurable changes in EV elasticity.

We develop a protocol comprising a theoretical framework, experimental technique, and statistical approach to accurately quantify the bending and elastic modulus of EVs. We show, that in contrast to previous reports (12), the EVs behave as surface-adhered vesicles showing a linear dependence of tether force on the tether length. We then apply our method to different EV populations derived from the human embryonic kidney (HEK293T) cell line and its genetically engineered versions with altered tetraspanin expression. The bending modulus estimated for the different EV families ranges from 15 to 33 $k_B T$ with large fluctuations within each family of vesicles which is consistent with inherent EV heterogeneity. Interestingly, our experiments also show large fluctuations of measured values even for a single EV when repeatedly examined under identical conditions. We suggest that such behavior is driven by both thermal and compositional effects, as expected for such nanoscale objects. We find that the probability distribution functions (PDFs) of elastic moduli are best described, not by a single Gaussian, but by a superposition of Gaussians. Consequently, commonly used techniques to test for statistical significance, e.g., the Student's t test can not be employed. We use the Jensen–Shannon divergence to differentiate between the PDFs. Our results suggest that protein alternations possibly do influence the elastic moduli of EVs, but they are often hidden in such large fluctuations.

1. Results

We performed force spectroscopy in a liquid environment (1×PBS) on EVs derived from HEK293T cell line. We followed the isolation method as described in ref. 14. To assess the influence of the protein alterations on the elastic properties of EVs, the expression of tetraspanins was genetically altered in the cell producing two different classes of EVs along with the wild type (WT-EVs): i) sample with CD63 knockout (CD63-KO) and ii) sample with CD9-CD63-CD81 knockout (Pan-KO). To assess the effect of protein corona, if any, we analyzed an additional sample type referred to as WT-SEC. To remove the protein corona, we followed an earlier report (15), and further processed WT-EVs with bind-elution size exclusion chromatography. Further details on sample preparation are presented in Section 4.3.

1.1. Shape of Adhered Vesicles. A typical topographical profile for an EV in a liquid environment measured by AFM is shown in Fig. 1*A*. Theories and experiments of adhesion of Giant Unilamellar Vesicles (GUVs) to glass cover slips (16–18) suggest that the shape of the vesicle would be that of a spherical cap. Earlier works (6, 8) on nanovesicles have also made the same assumption. The topographical profile is a height field H as a function of two-dimensional coordinates X and Y, typical examples are shown in Fig. 1*B*. The height field as a function of the slow axis of the scanning of the AFM—along the lines marked in Fig. 1*B*—is shown in Fig. 1*C*. We fit a circle to this profile taking into account the correction due to the shape of the tip of the AFM to determine the effective radius (R_c) of

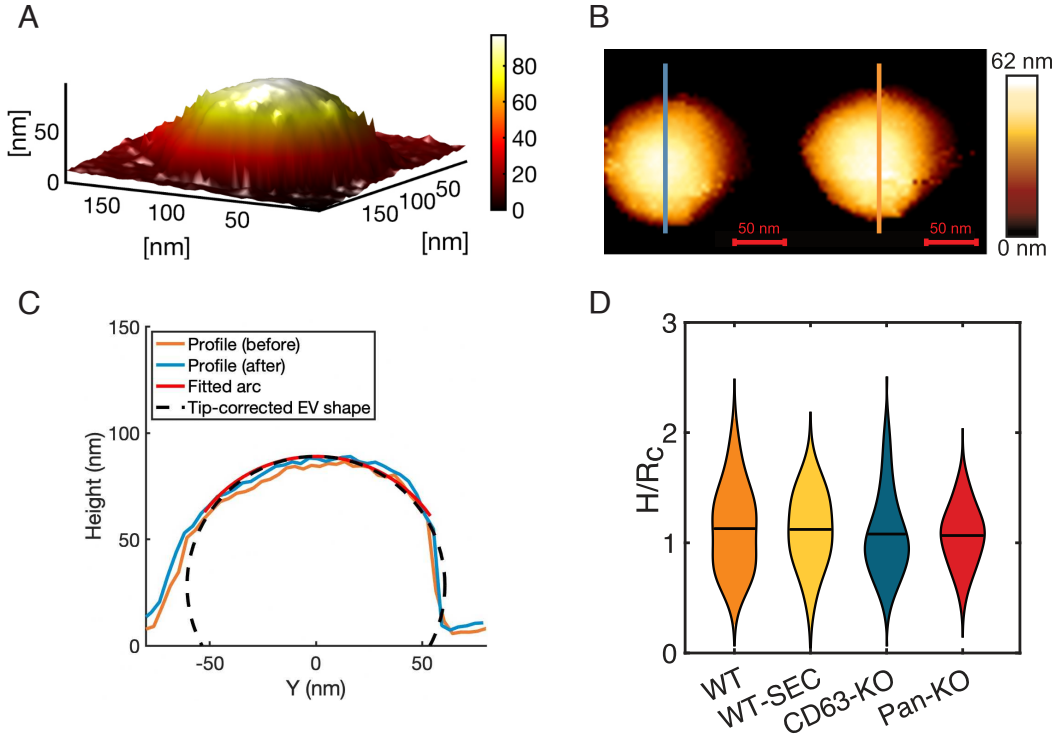

Fig. 1. Topographic image. (*A*) Topographic image of a single vesicle. (*B*) The height field plotted as a color for a typical vesicle before (*Left*) and after (*Right*) force spectroscopy. (*C*) The measured height, its fitted arc, and the tip-corrected EV shape extracted from the line shown in (*B*). (*D*) The ratio of the height and the radius of curvature. The horizontal black line indicates mean of the ratio. Mean for WT: 1.13, WT-SEC:: 1.12, CD63-KO: 1.08, and Pan-KO: 1.07.

the EV, as earlier described in ref. 8. We show in Fig. 1*C* the measured height, its fitted arc, and the tip-corrected EV shape for a typical example. Several additional examples are shown in *SI Appendix*, section 2. The probability distribution of the ratio H/R_c for all the vesicles is presented in Fig. 1*D*. A vesicle with $H/R_c > 2$ indicates a nonrealistic shape and was disregarded from future analysis. The radius R_c ranges from approximately 40 nm to 100 nm. Almost all of them fall within the class of small EVs (sEVs) defined (see e.g., ref. 19, page 9) to be less than 200 nm in diameter but a few do not. Hence, in the rest of this paper, we call them EVs.

For the measurement of force–distance curves, care is necessary. The EVs need to be immobile for the entire process, and the applied force and tip velocity must be small enough to avoid irreversible damage to the EVs. We image every EV twice—before and after the force spectroscopy—to make sure they are not damaged or have moved; see Fig. 1 *B* and *C*. In total, we imaged and performed force-spectroscopy on 49 vesicles of the WT family 39 of the WT-SEC family, 24 of CD63-KO family, and 18 of the Pan-KO family. We highlight two important experimental differences as compared to earlier studies (6, 12): a) the AFM-tip used in this study is smaller (radius $\leq$10 nm); and b) the maximum indentation force is also smaller at only 800 pN.

1.2. Force–Distance Measurements. In Fig. 2*A* we show a typical example of the force–distance curves. Here, we plot only the approach curves. As we repeat the experiment many times ($\approx$150) on the same EV, each time we obtain a different force–distance curve. To the best of our knowledge, this large variation in the force–distance curves is not seen in GUVs. Note that this variation is not originating from the AFM setup, as can be seen by repeating the same experiment but on a clean coverslip instead of an EV; see *SI Appendix*, section 5. We shall revisit these variations later. The average of all the force–distance curves is shown in red in Fig. 2*A*. We shall call this the average force–distance curve.

1.2.1. Theory. The EVs are similar to GUVs in the sense that both are a drop of fluid enclosed within a lipid bilayer (20). The two essential differences are as follows: i) the membrane of the EVs contains many other molecules, including proteins and cholesterol; and ii) the EVs are much smaller in size. Hence, we expect that the theory that describes the force–distance curves of EVs is similar to the theory applied to GUVs. Next, we present a summary of our theory—a more detailed description can be found in *SI Appendix*, section 10.

1. Typically, the force–distance experiments on cells, e.g., red blood cells are interpreted with Hertzian contact mechanics (21–24). Within this model, the cell is a deformable solid. At small distance d, the force F is given by $F \propto d^{3/2}$. The EVs cannot be modeled as solids because they lack the internal organelles and cytoskeleton of the cell.
2. The lipid bilayer (with the addition of proteins, nucleic acids, and glycans) of EVs is a (two-dimensional) fluid. It has zero shear modulus but a nonzero area modulus K_A. The usual thin-shell theory (21, 25, 26), which has also been generalized to pressurized shells (11, 27), includes (in-plane) shear modulus and is therefore not applicable to EVs. In other words, the shell in standard thin-shell theory is a two-dimensional solid whereas the lipid bilayer of EVs is a two-dimensional fluid.
3. Thus, the EVs must be modeled as shells but with fluid membranes, similar to the model of GUVs. We call this the Canham-Helfrich model. In this model, a deformation contributes to the change in energy in three possible ways: change in area, change in volume, and change in curvature or bending. Henceforth we use this model to interpret the force–distance curves.

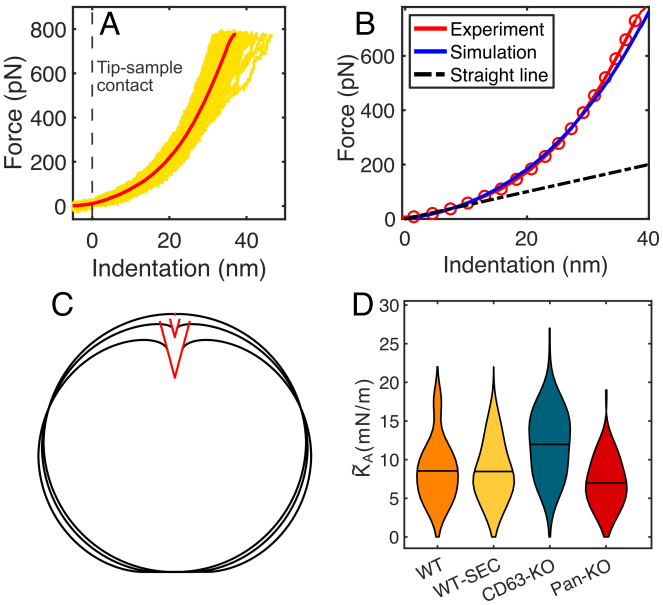

Fig. 2. Approach curves. (*A*) 150 indentation iterations on a vesicle (yellow lines). The average force–distance curve is shown in red. (*B*) The average indentation curve from (*A*) and the curve subject to the fitting of the model for $\kappa_A = 618.84\,\mathrm{mN\,m^{-1}}$ and $\Sigma_0 = 5.49\,\mathrm{mN\,m^{-1}}$ in the same scale. The dashed black line shows a linear fit at small distances. (*C*) The shape of the vesicle obtained from our simulations for three different values of the force $F = 2$, 90, and 600 pN respectively. The red triangle illustrates the conical tip with the half-cone angle of 15°. (*D*) The probability distribution functions, plotted as violin plots, of the $\bar{\kappa}_A$ of vesicles from the different families: WT, WT-SEC, CD63-KO, and Pan-KO. These are calculated from the average $\bar{\kappa}_A$ value for each vesicle. The horizontal black line indicates the mean.

Assuming that a reasonable estimate of the bending modulus of EVs is the typical bending modulus of lipid bilayers, it is possible to show that the contribution of bending to the change in energy is very small (6). Following the standard prescription for GUVs (28), we assume that the volume of the vesicle remains unchanged.

As this is a key assumption, where we differ from earlier work (6) on EVs we discuss this in some detail. The only way the volume can change is if water leaks out of the semipermeable membrane. Using existing data for the permeability of water through bilipid membranes, we find that within the time scale of the experiment, the leakage is negligible—the volume remains constant; see *SI Appendix*, section 10C. There is the additional possibility of water leaking out through transient but reversible pore formation, similar to what has been seen in GUVs (29–31). Ref. 31 shows that in GUVs pores form at a time interval of roughly 400 s. Let us assume that pores form in EVs at about the same time interval. For us, a single indentation takes 1 s. As these are very different timescales, we expect the pore formation not to play any significant role during a single force–distance measurement. Furthermore, if a pore had formed within the time interval it takes for our complete set of 150 measurements, we would expect a systematic change in the nature of force–distance curves before and after the pore formation. As we see no such change, we presume that pore formation does not play a significant role. Nevertheless, we believe this is a very interesting avenue for us to explore in our future publications. There is a

third possibility that the bilayer may have been penetrated by the AFM tip itself. Ref. 6 shows that this can happen but at forces that are significantly higher than the ones we have used. Thereby, we can also rule out the possibility of change of volume due to bilayer penetration by the AFM tip. Then the only possibility that remains is the change in area.

Let us consider the case where a small external force F generates a small deformation d. Let R_v be the effective radius of the vesicle defined by $(4/3)\pi R_v^3 \equiv V$, where V is the volume of the adhered vesicle. We consider $d \ll R_v$ such that d/R_v is a small parameter. Then the change in free energy can be estimated as (*SI Appendix*, section 10A)

$$\Delta\mathcal{F} \approx B_1 K_A d^2 - B_2 F d, \qquad [1]$$

where B_1 and B_2 are dimensionless constants that depend on the details of the indenter and the shape of the adhered vesicle and K_A is the in-plane area modulus of the membrane. The second term in the free energy is the work done by the indenting force. We have also assumed that the d is so small that it does not significantly change the adhesion energy of the EV to the bottom plate. Minimizing the free energy with respect to d and setting it to zero we obtain $F \propto K_A d$—a linear force–distance relationship. Note that thin-shell theory for pressurized shells also gives a linear force–distance relationship for small deformation (11, 27).

Unfortunately, the linear force–distance relationship for small deformation does not allow us to determine the elastic modulus K_A because the constant of proportionality, which depends on the adhered shape of the vesicle and the geometry of the indenter, can not be determined by the kind of dimensional arguments given here. Nevertheless, two vesicles with exactly the same surface molecules would have exactly the same interaction with the coverslip, and in all cases, we have used the AFM probe with the same geometry. Therefore, we can define an effective elastic modulus $\tilde{K}_A$ from the slope of the force–distance curve at small deformation. Although this approach does not allow us to measure the K_A accurately, it does allow us to measure the change in K_A as a result of knocking out of certain proteins. In Fig. 2*B* we show a typical example of the average force–distance curve (red line) together with a linear fit at small distances. The slope of the straight line gives $\tilde{K}_A$.

To fit the force–distance curve over a larger range, we need detailed numerical simulations. We follow ref. 32 who solved the same problem for GUVs, (*SI Appendix*, section 10). Again, the only free-energy cost that comes from deformation is due to change in area—the volume is assumed to be constant. The adherence of the vesicle is modeled by a prestress, Σ_0. By obtaining the best fit of the numerical solution of the model to the experimental data we can, in principle, find the two fit parameters, K_A and Σ_0. A typical example is shown in Fig. 2*B*. The pretension Σ_0 depends on the relative osmotic pressure of the vesicle to the medium, the strength of adhering forces, and the radius and the area modulus K_A of the vesicle (*SI Appendix*, section 10B). The numerical and the experimental force–distance curves agree well with each other not only at short distances but over almost the complete range of distances. This confirms that our choice of modeling is appropriate. Finally, the data also justify our assumption that the volume of the EVs remains constant.

1.2.2. Experiments. Returning to the experiments, we plot the average force–distance curve for a single vesicle in Fig. 2*B*. We find that there is indeed a small range of scale over which $F \propto d$. As the indentation progresses, the response becomes nonlinear. Next, we fit a straight line to the first 10% of the indentation (roughly equal to 50 data points) of every indentation's force–distance curve—not to the average force–distance curve). The slope of the straight line gives the effective modulus $\tilde{K}_A$ for each vesicle. The probability distribution functions of the average effective modulus $\tilde{K}_A$ of the families are plotted in Fig. 2*D* as violin plots. The mean and SD of the $\tilde{K}_A$ are 8.5 mN/m and 3.9 mN/m for the WT family, 8.5 mN/m and 3.7 mN/m for WT-SEC, 12.0 mN/m and 3.8 mN/m for CD63-KO, and 7.0 mN/m and 2.8 mN/m for Pan-KO, respectively. In comparison to the WT family, vesicles in the CD63-KO family have a higher mean $\tilde{K}_A$ while the Pan-KO family shows a lower mean $\tilde{K}_A$. Earlier studies (33–35) have reported similar effective elastic moduli of various EVs ranging from 7 mN/m up to 49 mN/m. These studies have all extracted the moduli in a similar way and on similar sample sizes. We have not found any earlier nanomechanical studies on EVs derived from HEK293T cells. To the best of our knowledge, the influence of knocking out certain proteins has not been studied before.

We do not expect any significant dependence of our results on the tip-size of the AFM because we extract $\tilde{K}_A$ from the regime of small deformation where the tip-size dependence is found to be minimal (6). For all the data reported here, the speed of the AFM tip is 200 nm/s. We have checked that doing the experiments at a faster, 500 nm/s, and slower speed, 100 nm/s, do not significantly change our conclusions; see *SI Appendix*, section 7. We also do not see any dependence of adhered shape with $\tilde{K}_A$; see *SI Appendix*, section 8.

The PDFs plotted in Fig. 2*D* suggests that they cannot be approximated by a single Gaussian. We calculate the PDFs using kernel density estimation with a Gaussian kernel. In other words, we find the superposition of Gaussian distributions that best fit our data. In *SI Appendix*, section 11 we plot both the histograms and the PDFs estimated by the kernel density estimation for all the families.

1.3. Variation of Effective Elastic Modulus. The PDFs show the inherent heterogeneity of the deformability of the EVs coming from all the different sample families. While the WT, WT-SEC, and Pan-KO families resemble each other in distribution shape, peak, and mean, the CD63-KO distribution shows deviations from the rest. Are the differences we see statistically significant? As the PDFs are not simple Gaussians, the Student's t test can not be employed here to test the statistical significance (36). Hence, we need a technique to distinguish between PDFs which are not Gaussian. Furthermore, note that we are dealing with small sample sizes in each family, hence the PDFs themselves are poorly determined. For most single vesicles, we obtain about 150 values of $\tilde{K}_A$. We plot them in Fig. 3*A*. The values are close to normally distributed but show significant variation; see also *SI Appendix*, section 6. Note that these values are decorrelated with one other. In Fig. 3*B* we present the range of values of $\tilde{K}_A$ that we obtain from individual force–distance curves for each of the families in barcode plots. The families WT and WT-SEC are close to each other although the former shows a larger span of $\tilde{K}_A$ values. The family CD63-KO has relatively high values of $\tilde{K}_A$ compared to the WT and the family Pan-KO seems to have relatively smaller values of $\tilde{K}_A$ compared to WT. At this stage, we consider for each family three PDFs of $\tilde{K}_A$ in the following manner. Let the average $\tilde{K}_A$ for a single vesicle be denoted by $\langle\tilde{K}_A\rangle$, and its SD $\Delta\tilde{K}_A$. Then we have one PDF each for $\langle\tilde{K}_A - \Delta\tilde{K}_A/2\rangle$, $\langle\tilde{K}_A\rangle$, and

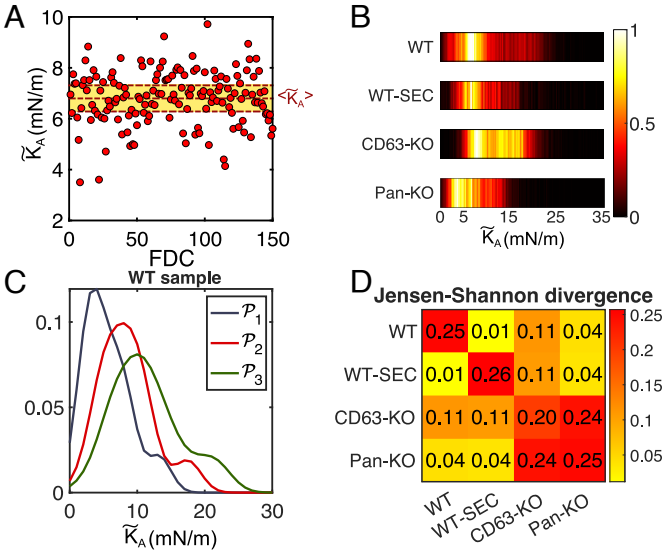

Fig. 3. Variations of $\tilde{K}_A$ in a single vesicle. (*A*) The many values of $\tilde{K}_A$ extracted from individual force–distance curve of a single vesicle. The shaded region indicates one SD and the central line shows the mean value. (*B*) Barcode plot of all values of $\tilde{K}_A$ for all the vesicles in each family. (*C*) $\mathcal{P}_1$, $\mathcal{P}_2$, and $\mathcal{P}_3$ of the WT sample. (*D*) Jensen–Shannon divergences between effective elastic modulus of the samples. The samples are internally compared across $\mathcal{P}_1$ and $\mathcal{P}_3$ (diagonal elements) while the distance across different samples (nondiagonal elements) compares $\mathcal{P}_2$ of the two samples.

$\langle \tilde{K}_A + \Delta\tilde{K}_A/2 \rangle$, we denote them respectively by $\mathcal{P}_1$, $\mathcal{P}_2$ and $\mathcal{P}_3$. In Fig. 3*C* we show that for the WT family.

To measure how two PDFs $p(x)$ and $q(x)$ differ from each other a commonly employed device is the Kullback–Leibler (KL) divergence (37).

$$D_{KL}\left(p \,\middle|\, q\right) \equiv \int dx p(x) \log\left(\frac{p(x)}{q(x)}\right). \qquad [2]$$

A straightforward interpretation is that the KL divergence is the relative entropy between two distributions. From the point of view of data science, the relative entropy can be considered to be the data required to reconstruct the target distribution q given the distribution p. It is defined to be strictly positive and is zero only when $p = q$ everywhere. But it is not symmetric in p and q, in other words, the $D_{KL}\left(p \,\middle|\, q\right) \neq D_{KL}\left(q \,\middle|\, p\right)$. A symmetric generalization is the Jensen–Shannon divergence defined by

$$D_{JS} \equiv \frac{1}{2}\left[D_{KL}\left(p \,\middle|\, \frac{p+q}{2}\right) + D_{KL}\left(q \,\middle|\, \frac{p+q}{2}\right)\right]. \qquad [3]$$

We use this as our parameter to measure the distance between two PDFs. We note that, although this is often used, there is no unique definition of the distance between two PDFs. The maximum value of the Jensen–Shannon divergence is unity. In what follows, we will not base any conclusion on the values of Jensen–Shannon divergence itself but its relative values, i.e., we will use the Jensen–Shannon divergence to find out which of the two PDFs q_1 and q_2 is close to the PDF p.

We measure the Jensen–Shannon divergence between $\mathcal{P}_1$ and $\mathcal{P}_3$ of one family and between $\mathcal{P}_2$ of two families and plot them as a matrix in Fig. 3*D*. The first $(1, 1)$, element of this matrix is the D_{JS} between $\mathcal{P}_1$ and $\mathcal{P}_3$ for the WT family. Similarly, all the diagonal elements show the same distance for each family. The off-diagonal elements show the distance between the $\mathcal{P}_2$ of two different families. By looking at the first column (or row) of this matrix, we see that for the WT family, the distance within the family is much more than the distance between this family and any other family. There is only one case where the distance within the family is less than the distance between the families—compare CD63-KO with Pan-KO. The distance between $\mathcal{P}_1$ and $\mathcal{P}_3$ within CD63-KO family is 0.20, whereas the distance between $\mathcal{P}_2$ of CD63-KO family with Pan-KO family is 0.24. This is the only case where we may claim that our method distinguishes one family from another, even then the difference between the distances is small. Note also that we find the distance between the WT family and the WT-SEC family is very small. As reported earlier (15), additional cleaning with SEC is expected to remove protein corona. Our results mean that either the effect of the protein corona on $\tilde{K}_A$ is negligible or (possibly more likely) that the sample preparation steps before the AFM study, which also involves several washing steps, already remove the corona. Another aspect to consider is the compositional heterogeneity of EVs derived from a cell line or even a single cell (38, 39). Such a variation may also result in a distribution of mechanical properties as we see in our case.

Note that we have not been able to determine K_A but an effective modulus $\tilde{K}_A$. In principle, using detailed numerical simulations, as described in *SI Appendix*, section 10B, it may be possible to determine K_A. But, in our experience, this method is too time-consuming to apply to individual force–distance curves. We have analyzed only a fraction of the average force–distance curves and have obtained excellent agreement between experiment and numerical simulations. Representative force–distance curves and their fits for each family are presented in *SI Appendix*, section 10B. As the number of samples measured in each family is small we have no hope of distinguishing between different families.

1.4. Measurement of Bending Modulus. In Fig. 4*A*, we show a typical recording of an approach and a retraction of the AFM tip. We have already used the approach curves to find out the effective area modulus $\tilde{K}_A$. In many cases, we find that the retraction curves show the behavior seen in Fig. 4*A*. This indicates the formation of a tether. The retrace curve showing tether formation for GUVs (28, 40) and cells (41) usually looks different: The force remains a (negative) constant as the length of the tether increases and eventually jumps back to zero as the tether is snapped. In such cases, minimization of the free energy gives the tether force to be $2\pi\sqrt{2\kappa\Sigma}$, where κ is the bending modulus and Σ is the membrane tension. Typically, this is observed in experiments in tube-pulling assays where the GUV is aspirated in a micropipette (the aspiration pressure sets the membrane tension) while a tether is pulled. Our experimental setup is different and we observe a different qualitative behavior—the force (F) changes as the length of the tether (L) increases, F/L remains approximately a constant (*SI Appendix*, section 9). The same behavior has already been calculated for adhered GUVs in ref. 9. The crucial difference between this and the tether formation in tube-pulling assays is that for the former the vesicle is not considered a quasi-infinite reservoir of lipids. This approach is appropriate for us because i) we consider adhered vesicles and ii) our vesicles are significantly smaller and thus, cannot be considered as a quasi-infinite reservoir of lipids. In general, the force–distance curves obtained in ref. 9 also depend on the adhesion forces between the vesicle and the base. By assuming the volume of the tether to be much smaller than the volume of the vesicle, following ref. 9, we obtain a

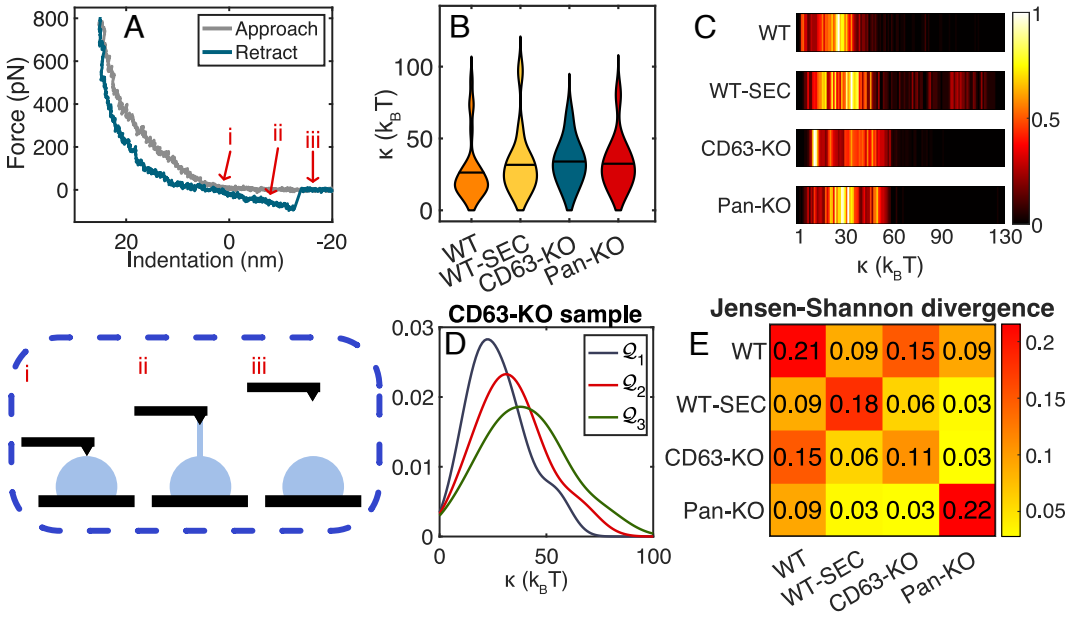

Fig. 4. Tether formation. (*A*) A typical force–distance curve with the approach (gray) and retract part (blue) which shows tether formation. The different stages of tether formation correspond to the points: i) AFM tip touches the vesicle ii) tip is removed, tether formed, and the area of contact between the vesicle and the substrate decreases, and iii) tether is snapped. (*B*) Violin plots of the bending modulus of EVs from the WT, WT-SEC, CD63-KO, and Pan-KO families. The black line indicates the mean. (*C*) Normalized heat map of all extracted bending moduli for all vesicles in each sample. Bar width: $1/k_B$. (*D*) $\mathcal{Q}_1$, $\mathcal{Q}_2$ and $\mathcal{Q}_3$ of the WT-SEC sample. (*E*) Jensen–Shannon divergences between effective bending modulus of the samples. The samples are internally compared across $\mathcal{Q}_1$ and $\mathcal{Q}_3$ (diagonal elements) while the distance across different samples (nondiagonal elements) compares $\mathcal{Q}_2$ of the two samples.

simplified force–distance relation:

$$\kappa \simeq \frac{R_c H}{4\pi}\left(1-\frac{H}{4R_c}\right)\left[1-\left(\frac{2R_c}{H}\right)^{\frac{1}{3}}\left(1-\frac{H}{4R_c}\right)^{-1}\right]\left(\frac{F}{L}\right). \quad [4]$$

We use this expression to obtain the bending modulus κ from each case of the force–distance plot involving tether formation. The PDFs of the bending modulus of the families are plotted in Fig. 4*B* as violin plots. In *SI Appendix*, section 12, we plot both the histograms and the PDFs estimated by the kernel density estimation for all the families. The tether formation does not happen every time the AFM tip is retracted, therefore the sample size from which the average κ is calculated is smaller than in the case of $\tilde{K}_A$. Note that, similar to what happened with the measurement of $\tilde{K}_A$, different tether formation experiments on the same vesicle yield different values for κ. In Fig. 4*C* we show a barcode plot for all the bending moduli measured for different families. While the CD63-KO family and Pan-KO have a smaller spread in their values, the WT-SEC family shows a larger spread. Earlier measurements of the bending modulus in EVs have obtained values somewhere between 2 and 20 $k_B T$ (12, 34, 35, 42). Bending modulus of lipid bilayers in GUVs have been measured to be in the range of 10 to 40 $k_B T$ depending on composition (43–47). The mean values of our measurements fall in the same range although, we find several values that are somewhat larger. Once again, the PDFs of our data are not single Gaussians. Hence, once again, we cannot employ the *t* test to check whether the differences between different families are statistically significant. We proceed in the same way as we have done for the measurement of $\tilde{K}_A$. The first step is to estimate the error in the measurement of κ. In Eq. **4**, the bending modulus depends on the height H and radius R_c of the vesicles and also the ratio F/L that we obtain from the force–distance curves. We assume that the errors in measuring H and R_c are small compared to the variation in F/L for different cases of tether formation. We attribute the source of error in κ to the variation in F/L, i.e.,

$$\Delta\kappa \simeq \frac{R_c H}{4\pi}\left(1-\frac{H}{4R_c}\right)\left[1-\left(\frac{2R_c}{H}\right)^{\frac{1}{3}}\left(1-\frac{H}{4R_c}\right)^{-1}\right]\Delta\left(\frac{F}{L}\right), \quad [5]$$

where we obtain $\Delta(F/L)$ from the SD of F/L over the many measurements of tether formations. Next, we construct three PDFs for each family, one each for $\langle\kappa\rangle-\Delta\kappa$, $\langle\kappa\rangle$, and $\langle\kappa\rangle+\Delta\kappa$, denoted by $\mathcal{Q}_1$, $\mathcal{Q}_2$, and $\mathcal{Q}_3$. The three PDFs for the CD63-KO family are shown in Fig. 4*D*. We again calculate the matrix of Jensen–Shannon distances and plot them in Fig. 4*E*. We find again that the diagonals of this matrix are typically larger than the off-diagonal values, i.e., the difference between the families is not statistically significant. The exception is again the family CD63-KO. The distance between $\mathcal{P}_1$ and $\mathcal{P}_3$ within CD63-KO family is 0.11, whereas the distance between $\mathcal{P}_2$ of CD63-KO family with WT family is 0.15, the PDF of bending modulus of CD63-KO is (marginally) statistically distinct from the PDF of bending modulus of the WT family.

2. Experiments on Liposomes

To develop a deeper understanding of the underlying mechanisms, we perform additional measurements on liposomes. We use liposomes with two different compositions varying in phospholipid lipid contents, cholesterol amount and inclusion of a peptide—see Section 4.4 (*Materials and Methods*) for details. We use an identical protocol for the surface

functionalization and force spectroscopy as followed for EVs. In *SI Appendix*, section 4 we show the result of our experiment on an individual liposome. For the first group, comprising fluid phase lipids with a cholesterol contents mimicking that of EVs, the variation of $\tilde{K}_A$ obtained from the force–distance curves are approximately the same as we observe for EVs. For small (0.5 nN) values of the maximum indenting force, the tether formation shows the same qualitative behavior as EVs: The force (F) changes as the length of the tether (L) increases, F/L remains approximately a constant; see *SI Appendix*, section 9B. But for higher force (1.25 nN) we find tether formation similar to tube-pulling assays for GUVs, *SI Appendix*, section 9B, but such a large force, typically, irreversibly damages the liposomes. For the second group of vesicles, comprising a gel phase lipid with a significantly smaller amount of cholesterol than found in EVs, we find that the variation of $\tilde{K}_A$ obtained from the force–distance curves are significantly smaller—about half.

3. Discussion

Several comments are now in order. The first concerns the theoretical model that we use to interpret the AFM measurements. We agree with earlier works (6, 12) that neither the Hertzian model nor the thin-shell theory is appropriate to analyze the AFM measurements. We also agree that the contribution from bending is negligible. We differ from refs. 6 and 12 in one crucial way: We assume the volume of EVs to be constant during indentation, while the area changes. We present three justifications. First, the EVs are very similar to GUVs except for their size—for GUVs, the analysis of force–distance data uses the same assumption. Second, we argue that over the time scale of one force–distance measurement very little change of volume due to the osmosis of water is possible (*SI Appendix*, section 10C). And, third, a straightforward dimensional argument applied to our model reproduces the linear force–distance relationship at short distance and our detailed numerical simulations produce a good fit with the experimental data. So the first take-home lesson of our work is that the large amount of already existing methods and results for GUVs are the best guide to understand the biomechanical properties of EVs with additional care necessary to take into account their small sizes and the fluctuations as we discuss next.

One crucial aspect of AFM measurement of force–distance curves of EVs that we particularly emphasize are their random variations. For a single EV, about 150 repeated measurements give force–distance curves that are quite different from one another; see Fig. 2*A*. This is a peculiar aspect of EVs—never observed in GUVs, to the best of our knowledge. An important point to note is that these fluctuations seem to be Gaussian and decorrelated with one another, see Fig. 3*A*, and they are present also in liposomes. We identify two possible mechanisms that can give rise to these fluctuations.

1. The thermal fluctuations: Naively, we may argue that thermal effects are not important because for lipid bilayers $(k_B T/\kappa) \approx 1/20$ is less than unity. Recent theoretical works (11, 48, 49) have demonstrated that in thin shells the dimensionless number that determines the importance of thermal effects is the elasto-thermal number, given by $(k_B T/\kappa)\sqrt{Y_{2d}R^2/\kappa}$, where Y_{2d} is the two-dimensional Young's modulus. These results cannot be directly applied to EVs because EVs have a fluid membrane whereas the thin-shell theory considers a solid membrane. Nevertheless, for EVs, we can define a similar elasto-thermal number by replacing Y_{2d} by K_A: ET $\equiv (k_B T/\kappa)\sqrt{K_A R^2/\kappa} \approx 5$, where we have used (44) $K_A \approx 200\,\mathrm{mN\,m^{-1}}$ and $\kappa \approx 10^{-19}$J, and $R = 100\,\mathrm{nm}$. The elasto-thermal number is larger than unity, hence we do expect thermal effects to be important.
2. The diffusion of membrane molecules: It is well known that membrane contains proteins and various lipid domains which can diffuse (50, 51). Let us first consider the protein molecules. The diffusion constant, D, is estimated to vary over a large range (52, table 1). Let us take a representative value (53) of $D \approx 1\,\mu\mathrm{m^2\,s^{-1}}$. The typical time scale of a complete force–distance measurement is about 1 s. Over that time scale a protein diffuses approximately over an area of $1\,\mu\mathrm{m}^2$, which is significantly larger than the surface area of the EVs. This implies that by a single force–distance measurement, we obtain some kind of average elastic modulus. Thus every force–distance measurement yields a slightly different value of elastic modulus. However, the estimate of D we have used may be inaccurate because: i) proteins on the surface of EVs are known to form clusters (54); ii) the value of D has been measured for almost flat surfaces (52), for example on surfaces of cells; iii) the interaction between the AFM tip and such clusters may affect their diffusion. Note also that if the characteristic time scale of diffusion of proteins slowed down so much that it became comparable to the typical time scale of a force–distance measurement, then we would expect some correlation between successive measurements. But we do not see this. The same argument applies mutatis mutandis to lipid domains in liposomes.

   Intriguingly, the fluctuations for one family of liposomes are approximately similar to the EVs, while for the other family, the fluctuations are about half. We list below a few key differences between the two families; see Section 4.4 for a detailed discussion. One, family A, commercially sourced, has a cholesterol content similar to EVs and the lipid bilayer is not in gel phase under experimental condition. In contrast, family B, made in-house, has significantly lower cholesterol content and the lipids are at a phase coexistence of liquid ordered phase and gel phase under experimental condition. Two, family A contains a relatively high proportion of DOPS, which is negatively charged under experimental condition (pH of 7.4), whereas the family B contains only lipids that are neutral at experimental conditions. We have therefore included a small amount of PEGylated lipid (DMPE-PEG2k) to mitigate for the risk of forming a subpopulations of bilamellar vesicles. Clearly, some part of the fluctuations depend on the chemical composition of the vesicles. The same theme could be further explored by using liposomes made with only one type of lipid. Unfortunately, in our experiments, liposomes with homogeneous composition—made only of DOPC—are not structurally stable enough to survive force spectroscopy by AFM.

In summary, we must attribute the fluctuations we observe to both thermal fluctuations and compositional heterogeneity. During the last couple of years, there have been several measurements of the nanomechanical properties of vesicles through atomic force microscopy (6, 33, 42, 55–58). Most of these rest on the assumption that one or few measurements on each vesicle is enough for a representative value. Here, we show explicitly and justify theoretically that this is not the case.

Note that another consequence of such protein diffusion is that if antibodies are used to capture the EVs, all the

complementary proteins may eventually diffuse to the substrate side, thus inducing some degree of bias to the compositional fluctuations. To reduce and possibly to eliminate such a scenario, we use electrostatics capture of EVs, as we described in our previous work (59). This approach makes the selection of EVs less biased.

The next remark is about tether formation. Typical theory of force–distance curves for tether formation in GUVs (40) and cells (41) shows that the force remains a constant as the length of the tether increases and eventually jumps back to zero as the tether is snapped. Typically, this is observed in experiments in tube-pulling assays where the surface tension of the membrane is held constant. Nevertheless, the same theory has been used to interpret tether formation of adhered cells (60) and vesicles (8, 12, 28, 34) in which case the surface tension cannot be controlled. In our experiments, neither can we control the surface tension—a direct consequence of adhering the vesicles—nor can we assume that the EVs have a reservoir of lipids due to their small sizes. We obtain a linear force–distance relationship. We follow ref. 9, whose theory gives a linear force–distance relationship which we use to measure the bending modulus. To the best of our knowledge, there has been only one experimental measurement (10) of tether formation in GUVs that found a linear force–distance relationship although ref. 10 suggested a theoretical interpretation different from ref. 9. The linear force–distance in tether formation is also found in bacteria (61), and fibroblasts (62), but in these cases, the mechanism may be different. To summarize, ours is the first experimental observation of a linear force–distance relationship which may be interpreted using the theory of ref. 9.

Note also the natural heterogeneity of biomechanical properties within a family of EVs. Our data show that the PDF of the elastic modulus is not likely to be Gaussian but can be best represented by a superposition of several Gaussians. From the biological point of view, this is expected, because EVs are known to be heterogeneous containing several different subpopulations, each of which may generate a Gaussian distribution of biomechanical properties. This absence of simple Gaussianity also demands statistical methods that are suitable for families of EVs. As the underlying normality assumption is violated, we use the concept of Jensen–Shannon divergences to differentiate between probability distributions. We believe this is better suited as a statistical approach due to the natural variations of the elastic moduli of EVs.

Now let us discuss to what extent our original intention, v.i.z., to differentiate EV subpopulations based on their elastic properties, has been served. Membrane protein-based discrimination of EV subpopulations is by far the most investigated topic in the field, thus also providing the basis for our primary question, v.i.z., does the deformability of EVs depend on their membrane protein composition? We investigate this question by knocking out three tetraspanins which are highly abundant in HEK293T-derived EVs (63), thus they become an obvious choice for our experimental design. Note that knocking out of certain proteins may also have unwanted consequences where the proteins are replaced by other proteins or lipids. For example, it may change the cholesterol content of the EVs (64), which in turn can change their elastic properties, (see, e.g., refs. 65 and 66). Furthermore, ref. 67 has suggested that the presence of proteins may change the local curvature of the lipid membrane thereby changing its elastic properties (67). Our results suggest that in most cases, the natural variation in the elastic moduli within a family is too large to detect statistically significant changes, induced by protein alteration, between families. The only exception is the CD63 KO family, which shows some statistical difference. In particular, the $\tilde{K}_A$ of the CD63 KO sample is statistically different from the Pan-KO, while the bending modulus of CD63 KO is statistically different from the WT sample. If we look at just the mean values of the PDFs plotted in Fig. 2*D* we may think that the CD63 KO is indeed different from WT, WT-SEC, and Pan-KO. A recent paper (64) also reached the same conclusion based on only the mean value. But our careful and detailed statistical analysis shows that the difference between CD63 and WT (and WT-SEC) are not statistically significant. The only statistically significant difference is between CD63-KO and Pan-KO. A priori, this is counterintuitive because in Pan-KO, three tetraspanins including CD63 are knocked out. A way to understand this may go as follows. It has been established that, in general, knocking out tetraspanins gives rise to inclusion of alternative tetraspanins which are able to compensate for the effect of removing individual tetraspanins (68). But a recent paper (64) showed that CD63 is special—knocking it out gives rise to very minor changes to other proteins although cholesterol content is significantly changed. This may explain why the CD63-KO family is different from all the other three families, WT, WT-SEC, and Pan-KO. But the statistical fluctuations do not allow us to detect these differences, the only statistically significant conclusion we can reach is that the effective K_A of CD63-KO is statistically different from the Pan-KO, while the bending modulus of CD63 KO is statistically different from WT. Thus we must emphasize the second take-home message of our paper, to distinguish statistically significant changes between the properties of families of EV it is not sufficient to look at only the mean value—the complete PDF must be taken into account. The final take-home message of our work is that the error in earlier experiments may have been underestimated.

The study of the nanomechanical properties of extracellular vesicles is still in the early stages. The central goal of our paper is to address one of its greatest challenges: to properly identify stable and relevant protocols of analysis of EVs.

4. Materials and Methods

4.1. Chemicals and Materials. High-purity deionized water (DIW) with a resistivity of 18 MΩ cm was used throughout all the experiments. Casein (C5890) in powder, phosphate-buffered saline (PBS; P4417) in tablets, and poly-l-lysine (PLL; P2636) were purchased from Sigma-Aldrich (Burlington, MA, United States). The liposomes of family A were obtained from Liposoma BV, The Netherlands, and the family B was produced in-house. For in-house formulated liposomes, DPPC (850355C) and DMPE-PEG2k (880150P) were purchased from Avanti Polar Lipids (Alabaster, AL, United States), cholesterol (C8667) was purchased from Sigma-Aldrich (Burlington, M.A., United States), and PBS was purchased from Gibco (14190144).

4.2. Cell Culture and Extraction, Purification, and Isolation of EVs. HEK293T (human embryonic kidney-293T) cells were propagated in Dulbecco's modified Eagle's medium containing Glutamax-I and sodium pyruvate; 4.5 g/L Glucose; Invitrogen) supplemented with 10% fetal bovine serum (FBS; Invitrogen) and 1% Antibiotic–Antimycotic (Anti-Anti; ThermoFisher Scientific). In addition, 48 h prior to collection of conditioned media for EV isolation from HEK293T cells, cells were washed with PBS and the medium was changed to OptiMem (Invitrogen) (69). HEK293T-CD63KO and HEK293T-PAN-KO (CD9, CD63, and CD81) cell lines were generated by the delivery of Cas9-gRNA ribonucleoproteins (Integrated DNA Technologies, Coralville) targeting respective tetraspanin sequences using RNAiMAX (Thermo Fisher Scientific, Waltham, MA, USA). Shortly, 10,000 cells per well were seeded in a 96-well plate and treated after 24 h with 100 ng of Cas9-RNAiMax per well, following the protocol of Chesnut et al 2015 (70). Three days after treatment the cells were

stained with anti-CD63-APC or a mixture of anti-CD9/63/81-APC antibodies (14), and successfully edited cells were sorted on a BD Fusion flow cytometric cell sorter as single cells per well into 96-well plates. The resulting colonies were validated and expanded as stable cell lines. All cell lines were grown at 37 °C, 5% CO2 in a humidified atmosphere and regularly tested for the presence of mycoplasma. For EV preparation, cell culture-derived conditioned medium (CM) was first precleared from cells and debris by low-speed centrifugation (700 × *g* for 5 min) and subsequent centrifugation at 2,000 × *g* for 20 min to remove larger particles and debris. Next, medium was filtered through 0.22 μm bottle top vacuum filters (Corning, cellulose acetate, low protein binding) to remove any larger particles. Precleared CM was subsequently concentrated via tangential flow filtration (TFF) by using the KR2i TFF system (SpectrumLabs) equipped with modified polyethersulfone (mPES) hollow fiber filters with 300 kDa membrane pore size (MidiKros, 370 cm^2 surface area, SpectrumLabs), at a flow rate of 100 mL/min (transmembrane pressure at 3.0 psi and shear rate at 3,700 s^{-1}, as described previously (71). WT-SEC EVs were additionally purified by bind-elute size exclusion chromatography (BE-SEC): CM were concentrated by TFF as described above and then loaded onto BE-SEC columns (HiScreen Capto Core 700 column, GE Healthcare Life Sciences), connected to an ÄKTAstart chromatography system (GE Healthcare Life Sciences) as described previously (71). Amicon Ultra-0.5 10 kDa MWCO spin-filters (Millipore) were used to concentrate the sample to a final volume of 100 μL. EVs were stored in Maxymum Recovery polypropylene 1.5 mL tubes (Axygen Maxymum Recovery, Corning, cat MCT-150-L-C) in PBS-HAT buffer (PBS, 25 mM Trehalose, 25 mM HEPES, 0.2% Human Serum Albumin) before usage as described previously (14). Prepared sEV samples were characterized by Nanoparticle tracking analysis (NTA) to determine particle size and concentration using the NanoSight NS500 instrument equipped with NTA 2.3 analytical software and an additional 488 nm laser (71). The samples were diluted in 0.22 μm filtered PBS to an appropriate concentration before being analyzed. At least five 30-s videos were recorded per sample in light scatter mode with a camera level of 11 to 13. Software settings were kept constant for all EV measurements (screen gain 10, detection threshold 7). The analysis was performed with the screen gain at 10 and the detection threshold at 7 for all EV measurements. Successful knockout of CD63 and CD9/CD63/CD81, respectively, were validated by multiplex bead-based EV flow cytometry (Section 4.5) and single EV imaging flow cytometry (Section 4.6).

4.3. EV Sample Preparation. After purification and isolation, the EVs were adhered to coverslips. The coverslips were cleaned from organic residue with a 5:1:1 RCA-1 solution of deionized water, NH_3, and H_2O_2 (90 °C, 10 min). After cleaning, the coverslips were coated with 0.001% poly-l-lysine for 90 s. 100 μL of 1 × 10^9 part/mL of the sample suspended in 1×PBS was then incubated for 1 h at room temperature. A cut-up four-well insert (80,469, ibidi GmbH, Gräfelfing, BY, DE) was used to limit the spatial spread of the EV sample on the coverslip. After incubation, the substrate was thoroughly washed with 1×PBS. To reduce the risk of unsolved salt crystals contaminating scans, the PBS was filtered through a 0.2 μm PTFE filter (514-0070; VWR; AB, SE). Before loading the sample on the AFM, the liquid volume was increased to approximately 400 μL to avoid drying out the sample and deflating the vesicles during imaging. The dried-up sample showed up either as great spikes in the topographical image or as elongated, short vesicles (*SI Appendix*, section 13).

4.4. Composition and Preparation of Liposomes. The liposomes of family A are from a commercial source (Liposoma BV, The Netherlands). The liposomes have total lipid concentration of 16.7 ± 0.3 mg/mL, at a molar ratio of 30:23:47 DMPC:DOPS:cholesterol. They also contain a proprietary peptide.

The liposomes of family B are produced in-house. They contain DPPC: cholesterol:DMPE-PEG2k mole ratio of 85:15:1. They were formulated using the thin film hydration method (72). Chloroform solutions (5 to 10 mg/mL stock solutions) of the component lipids were mixed in a 1.5 mL glass vial to give the required mole ratios, resulting in a total of 1 mg of lipid. Chloroform was evaporated overnight (≈16 h) at room temperature. The film was subsequently hydrated with 1 mL PBS, followed by heating to 55 °C, incubation at 55 °C for 30 mins, agitation on a vortex shaker (6 × 10 s at 55 °C) and extrusion 35 times at 55 °C over a 100 nm polycarbonate membrane (Whatman Nucleopore Track-Edged Membranes) using an Avanti Mini-Extruder. The size distribution of the liposomes of family B and their key differences with the family A are presented in *SI Appendix*, section 3.

4.5. Multiplex Bead-Based EV Flow Cytometry. The EV surface marker composition and abundance for the tetraspanins CD9, CD63, and CD81 were assessed on respective EV samples by multiplex bead-based EV flow cytometry (MACSPlex EV Kit IO, Miltenyi Biotec) as described before (73, 74). Briefly, prepared EV samples (assay input dose: 1 × 10^9 NTA-based particles) were diluted with MACSPlex buffer to a final volume of 60 μL and incubated overnight with 10 μL MACSPlex Exosome Capture Beads on an orbital shaker at room temperature (RT) in the dark. Beads were washed with MACSPlex buffer, and then 4 μL of APC-conjugated CD9, CD63, and CD81 (Pan tetraspanin) detection antibodies were added to each sample, respectively, in a total volume of 135 μL. Following incubation for 1 h on an orbital shaker at RT, samples were washed again and incubated for another 15 min before a final washing step was performed. Incubation and washing steps were performed in 0.22 μm filter plates. Final samples were resuspended in 150 μL MACSPlex buffer and acquired on a MACSQuant Analyzer 10 flow cytometer (Miltenyi Biotec). Data were analyzed with FlowJo software version 10.5.3 and expressed as $\log_{10}$-transformed fold change values over respective non-EV containing buffer controls as described before (75). The heat map was generated with Morpheus (https://software.broadinstitute.org/morpheus). The relevant data are presented in *SI Appendix*, section 1.

4.6. Single EV Imaging Flow Cytometry. For single EV analysis experiments by Imaging Flow Cytometry (IFCM), EV samples were diluted in PBS-HAT (DBPS supplemented with 25 μM HEPES, 0.2% human albumin and 25 μM trehalose) (76) to a final concentration of 1 × 10^{10} particles/mL before usage. A volume of 25 μL (equivalent to 2.5 × 10^8 particles) was incubated with either CD63-APC antibodies or a mixture of CD9/CD63/CD81-APC antibodies (Pan-tetraspanin; CD9-APC, Miltenyi Biotec 130-103-956, lot 5200907825; CD63-APC, Miltenyi Biotec 130-100-182; lot 5200907851; CD81-APC, Beckman Coulter A87789, lot 200038) at a final respective antibody concentration of 4 nM overnight. Post staining, samples were diluted 1:10,000 in PBS-HAT before acquisition on a Cellstream instrument (Amnis/Cytek) with FSC turned off, SSC laser set to 40%, and all other lasers set to 100% of the maximum power. Small EVs were defined as SSC(low) by using CD63-mNeonGreen (mNG)-tagged EVs as biological reference material as described before (77), and regions to quantify fluorescence-positive populations were set according to unstained samples. Samples were acquired for 5 min at a flow rate of 3.66 μL/min (setting: slow) with CellStream software version 1.2.3 and analyzed with FlowJo Software version 10.5.3 (FlowJo, LLC). Dulbecco's PBS pH 7.4 (Gibco) was used as sheath fluid. Fluorescence calibration was performed as described previously (77). In brief, FITC MESF beads (Quantum FITC-5 MESF, Bangs Laboratories Inc., cat 555A, lot 13734) and APC MESF beads (Quantum APC MESF, Bangs Laboratories Inc., cat 823A, lot 13691) with known absolute fluorescence values for each bead population were acquired with the same settings used for EV measurements with the exception that the SSC laser was turned off, and linear regressions were performed to convert fluorescence values into FITC/APC MESF values, respectively. Flow cytometric plots using MESF unit axes were created with FlowJo v10.5.3. The relevant data are presented in *SI Appendix*, section 1.

4.7. AFM. The biophysical measurements were performed with a NanoWizard 3 BioScience AFM from JPK (Berlin, BE, Germany). A CoverslipHolder from Bruker was used to enable a liquid environment. Performing measurements in 1×PBS allows a higher preservation of their spherical shape than measurements performed in air (78). Qp-BioAC cantilevers from NanoAndMore GMBH (Wetzlar, HE, Germany) with nominal spring constants of 0.06 N/m, 0.1 N/m, and 0.3 N/m were used. For the study, we used AFM-tip of radius ≤ 10 nm and a maximum indentation force of 800 pN. All sessions started using the cantilever with the lowest nominal spring constant which was swapped to the other cantilever as tip contamination occurred. Before imaging the spring constant of the cantilever was determined through the thermal noise method (79). Images were obtained in Quantitative Image (QI) mode with an imaging force of 200 pN. First, a coarse scan of a 10 μm × 10 μm large region with a resolution of 39 nm/pixel was carried out. Objects with height greater than 25 nm and width greater than 100 nm at

this resolution were classified as potential EVs. For this, a 500 nm × 500 nm or 400 nm × 400 nm scan centered around the object at a resolution of 3.9 or 4 nm pixel^{-1} was considered. If the object exhibited a spherical cap shape it was assumed to be a vesicle, and force spectroscopy measurements were performed at its center. The force spectroscopy measurements were carried out with the maximum indentation force of 0.8 nN. At least 150 consecutive indentations were performed at the constant speed of 200 nm/s. After the set of force spectroscopy measurements, the vesicle was imaged again to ensure that the measurements had not damaged, deformed, or otherwise moved the vesicle.

4.8. Post Data Capture Processing. In Gwyddion, all single EV images were tilt-corrected and shifted in the z-direction to let the lowest pixel represent zero level. A line profile in the slow scan direction over the EV peak was exported to Matlab where a script calculated a radius of curvature (R_c) by fitting a circle to all the points with heights greater than half the maximum height as previously suggested in ref. 6. In the same protocol, Vorselen et al., suggest applying forces in the 5 to 10 nN range to completely indent the vesicle and reach the substrate. This allows the height, H, of the vesicle to be extracted from the force–distance curve instead of through the topographical images. However, such large forces are likely to rupture the vesicles and we avoid this step. Instead, the height was extracted from the line profile over the center of the EV.

4.9. Force Distance Curve Analysis. The force–distance curves were processed in the JPK Data Processing program. First, the offset and the tilt of the baseline were corrected. After this, the contact point between the AFM tip and the vesicle was found. Finally, the height was corrected for cantilever bending. A successfully processed curve would have its contact point at 0 nm indentation, and a constant baseline around 0 pN. The retract curves were exported to Matlab where a script identified curves with tether formations and extracted their length and force magnitude. The set of selection rules for the force–distance curves are given in *SI Appendix*, section 14.

Data, Materials, and Software Availability. Codes, EV measurements, and simulation data have been deposited in Zenodo (80).

ACKNOWLEDGMENTS. F.S., H.K., P.M., and A.D. acknowledge the financial support of the Erling-Persson Family Foundation, Swedish Research Council through grant 2018-06228 and Stockholm County Council through grant FoUI-966345. A.D. and M.T.G. also acknowledge financial support from VINNOVA through grant 2024-02197. V.P., V.A., and D.M. acknowledge the financial support of the Swedish Research Council through grants 638-2013-9243 and 2016-05225. D.M. thanks Sreekanth Manikandan and Kheya Sengupta for the discussions. NORDITA is partially supported by NordForsk. A.G. is an International Society for Advancement of Cytometry Marylou Ingram Scholar 2019-2024 and supported by a Karolinska Institutet Network Medicine Alliance Collaborative Grant. D.M. and A.D. express their gratitude for the valuable comments and suggestions provided by the anonymous reviewers and Dr. Anjali Sharma.

Author affiliations: [a]Department of Applied Physics, Kungliga Tekniska Högskolan Royal Institute of Technology, Stockholm 11419, Sweden; [b]Nordita, Kungliga Tekniska Högskolan Royal Institute of Technology and Stockholm University, Stockholm 11419, Sweden; [c]Department of Electrical Engineering, Uppsala University, Uppsala 75237, Sweden; [d]Division of Applied Electrochemistry, Kungliga Tekniska Högskolan Royal Institute of Technology, Stockholm 11419, Sweden; [e]Department of Physics, Stockholm University, Stockholm 11419, Sweden; [f]Department of Materials Science and Engineering, Northwestern University, Evanston, IL 60208; [g]Department of Laboratory Medicine, Division of Biomolecular and Cellular Medicine, Karolinska Institutet, Stockholm 17177, Sweden; [h]Department of Cellular Therapy and Allogeneic Stem Cell Transplantation, Karolinska University Hospital Huddinge and Karolinska Comprehensive Cancer Center, Stockholm 17177, Sweden; [i]Institute for Transfusion Medicine, University Hospital Essen, University of Duisburg-Essen, Essen 45147, Germany; [j]Breast Center, Karolinska Comprehensive Cancer Center, Karolinska University Hospital, Stockholm 75105, Sweden; [k]Karolinska Advanced Therapy Medicinal Products Center, ANA Futura, Huddinge 17177, Sweden; and [l]Division of Chemical Biology, Department of Life Sciences, Chalmers University of Technology, Gothenburg 41296, Sweden

1. E. I. Buzas, B. György, G. Nagy, A. Falus, S. Gay, Emerging role of extracellular vesicles in inflammatory diseases. *Nat. Rev. Rheumatol.* **10**, 356–364 (2014).
2. A. F. Hill, Extracellular vesicles and neurodegenerative diseases. *J. Neurosci.* **39**, 9269–9273 (2019).
3. D. W. Hagey *et al*., The cellular response to extracellular vesicles is dependent on their cell source and dose. *Sci. Adv.* **9**, eadh1168 (2023).
4. C. Bagci *et al*., Overview of extracellular vesicle characterization techniques and introduction to combined reflectance and fluorescence confocal microscopy to distinguish extracellular vesicle subpopulations. *Neurophotonics* **9**, 021903–021903 (2022).
5. B. Ma *et al*., Optical imaging of single extracellular vesicles: Recent progress and prospects. *Chem. Biomed. Imaging* **2**, 27–46 (2023).
6. D. Vorselen, F. C. MacKintosh, W. H. Roos, G. J. Wuite, Competition between bending and internal pressure governs the mechanics of fluid nanovesicles. *ACS Nano* **11**, 2628–2636 (2017).
7. A. C. Anselmo, S. Mitragotri, Impact of particle elasticity on particle-based drug delivery systems. *Adv. Drug Deliv. Rev.* **108**, 51–67 (2017).
8. D. Vorselen, M. C. Piontek, W. H. Roos, G. J. Wuite, Mechanical characterization of liposomes and extracellular vesicles, a protocol. *Front. Mol. Biosci.* **7**, 139 (2020).
9. A. S. Smith, E. Sackmann, U. Seifert, Pulling tethers from adhered vesicles. *Phys. Rev. Lett.* **92**, 208101 (2004).
10. D. Cuvelier, N. Chiaruttini, P. Bassereau, P. Nassoy, Pulling long tubes from firmly adhered vesicles. *Europhys. Lett.* **71**, 1015 (2005).
11. J. Paulose, G. A. Vliegenthart, G. Gompper, D. R. Nelson, Fluctuating shells under pressure. *Proc. Natl. Acad. Sci. U.S.A.* **109**, 19551–19556 (2012).
12. D. Vorselen *et al*., The fluid membrane determines mechanics of erythrocyte extracellular vesicles and is softened in hereditary spherocytosis. *Nat. Commun.* **9**, 4960 (2018).
13. Y. Feng *et al*., Nanomechanical signatures of extracellular vesicles from hematologic cancer patients unraveled by atomic force microscopy for liquid biopsy. *Nano Lett.* **23**, 1591–1599 (2023).
14. A. Görgens *et al*., Identification of storage conditions stabilizing extracellular vesicles preparations. *J. Extracell. Vesicles* **11**, e12238 (2022).
15. M. Wolf *et al*., A functional corona around extracellular vesicles enhances angiogenesis, skin regeneration and immunomodulation. *J. Extracell. Vesicles* **11**, e12207 (2022).
16. U. Seifert, R. Lipowsky, Adhesion of vesicles. *Phys. Rev. A* **42**, 4768 (1990).
17. K. Sengupta, L. Limozin, Adhesion of soft membranes controlled by tension and interfacial polymers. *Phys. Rev. Lett.* **104**, 088101 (2010).
18. K. Sengupta, A. S. Smith, "Measuring giant unilamellar vesicle adhesion" in *The Giant Vesicle Book*, R. Dimova, C. M. Marques, Eds. (CRC Press, 2019), pp. 381–399.
19. C. Théry *et al*., Minimal information for studies of extracellular vesicles 2018 (MISEV2018): A position statement of the international society for extracellular vesicles and update of the MISEV2014 guidelines. *J. Extracell. Vesicles* **7**, 1535750 (2018).
20. L. van der Koog, T. B. Gandek, A. Nagelkerke, Liposomes and extracellular vesicles as drug delivery systems: A comparison of composition, pharmacokinetics, and functionalization. *Adv. Healthcare Mater.* **11**, 2100639 (2022).
21. L. Landau, E. Lifshitz, *Theory of Elasticity, Course of Theoretical Physics* (Pergamon Press Ltd., Oxford, England, 1970), vol. 7.
22. K. E. Bremmell, A. Evans, C. A. Prestidge, Deformation and nano-rheology of red blood cells: An AFM investigation. *Colloids Surf. B: Biointerfaces* **50**, 43–48 (2006).
23. M. Li *et al*., Atomic force microscopy imaging and mechanical properties measurement of red blood cells and aggressive cancer cells. *Sci. China Life Sci.* **55**, 968–973 (2012).
24. V. Sergunova *et al*., Investigation of red blood cells by atomic force microscopy. *Sensors* **22**, 2055 (2022).
25. A. V. Pogorelov, *Bendings of Surfaces and Stability of Shells* (American Mathematical Soc., 1988), vol. 72.
26. W. Roos, R. Bruinsma, G. Wuite, Physical virology. *Nat. Phys.* **6**, 733–743 (2010).
27. D. Vella, A. Ajdari, A. Vaziri, A. Boudaoud, The indentation of pressurized elastic shells: From polymeric capsules to yeast cells. *J. R. Soc. Interface.* **9**, 448–455 (2012).
28. A. Janshoff, "Atomic force microscopy of giant unilamellar vesicles" in *The Giant Vesicle Book*, R. Dimova, C. M. Marques, Eds. (CRC Press, 2019), pp. 305–317.
29. O. Sandre, L. Moreaux, F. Brochard-Wyart, Dynamics of transient pores in stretched vesicles. *Proc. Natl. Acad. Sci. U.S.A.* **96**, 10591–10596 (1999).
30. F. Brochard-Wyart, P. G. de Gennes, O. Sandre, Transient pores in stretched vesicles: Role of leak-out. *Phys. A: Stat. Mech. Appl.* **278**, 32–51 (2000).
31. M. Pinot *et al*., Feedback between membrane tension, lipid shape and curvature in the formation of packing defects. bioRxiv [Preprint] (2018). https://doi.org/10.1101/389627 (Accessed 13 August 2018).
32. E. Schäfer, M. Vache, T. T. Kliesch, A. Janshoff, Mechanical response of adherent giant liposomes to indentation with a conical AFM-tip. *Soft Matter* **11**, 4487–4495 (2015).
33. F. Royo *et al*., Differences in the metabolite composition and mechanical properties of extracellular vesicles secreted by hepatic cellular models. *J. Extracell. Vesicles* **8**, 1575678 (2019).
34. R. Sorkin *et al*., Nanomechanics of extracellular vesicles reveals vesiculation pathways. *Small* **14**, 1801650 (2018).
35. S. Ye *et al*., Quantitative nanomechanical analysis of small extracellular vesicles for tumor malignancy indication. *Adv. Sci.* **8**, 2100825 (2021).
36. S. Boslaugh, *Statistics in a Nutshell: A Desktop Quick Reference* (O'Reilly Media, Inc., 2012).
37. P. Mehta *et al*., A high-bias, low-variance introduction to machine learning for physicists. *Phys. Rep.* **810**, 1–124 (2019).
38. M. Tong *et al*., Proteomic characterization of macro-, micro-and nano-extracellular vesicles derived from the same first trimester placenta: Relevance for feto-maternal communication. *Hum. Reprod.* **31**, 687–699 (2016).
39. C. Lässer, S. C. Jang, J. Lötvall, Subpopulations of extracellular vesicles and their therapeutic potential. *Mol. Asp. Med.* **60**, 1–14 (2018).
40. C. Prevost, M. Simunovic, P. Bassereau, "Creating membrane nanotubes from giant unilamellar vesicles" in *The Giant Vesicle Book*, R. Dimova, C. M. Marques, Eds. (CRC Press, 2019), pp. 365–376.
41. R. Phillips, J. Kondev, J. Theriot, H. Garcia, *Physical Biology of the Cell* (Garland Science, 2012).
42. A. Ridolfi *et al*., AFM-based high-throughput nanomechanical screening of single extracellular vesicles. *Anal. Chem.* **92**, 10274–10282 (2020).
43. V. Heinrich, R. E. Waugh, A piconewton force transducer and its application to measurement of the bending stiffness of phospholipid membranes. *Ann. Biomed. Eng.* **24**, 595–605 (1996).

44. W. Rawicz, K. C. Olbrich, T. McIntosh, D. Needham, E. Evans, Effect of chain length and unsaturation on elasticity of lipid bilayers. *Biophys. J.* **79**, 328–339 (2000).
45. N. Fa *et al*., Decrease of elastic moduli of DOPC bilayers induced by a macrolide antibiotic, azithromycin. *Biochim. Biophys. Acta Biomembranes* **1768**, 1830–1838 (2007).
46. H. Seto, N. Yamada, M. Nagao, M. Hishida, T. Takeda, Bending modulus of lipid bilayers in a liquid-crystalline phase including an anomalous swelling regime estimated by neutron spin echo experiments. *Eur. Phys. J. E* **26**, 217–223 (2008).
47. J. F. Nagle, Experimentally determined tilt and bending moduli of single-component lipid bilayers. *Chem. Phys. Lipids* **205**, 18–24 (2017).
48. A. Košmrlj, D. R. Nelson, Statistical mechanics of thin spherical shells. *Phys. Rev. X* **7**, 011002 (2017).
49. V. Agrawal, V. Pandey, D. Mitra, Active buckling of pressurized spherical shells: Monte carlo simulation. *Phys. Rev. E* **108**, L032601 (2023).
50. P. S. Niemela *et al*., Membrane proteins diffuse as dynamic complexes with lipids. *J. Am. Chem. Soc.* **132**, 7574–7575 (2010).
51. S. Ramadurai *et al*., Lateral diffusion of membrane proteins. *J. Am. Chem. Soc.* **131**, 12650–12656 (2009).
52. A. Kusumi *et al*., Paradigm shift of the plasma membrane concept from the two-dimensional continuum fluid to the partitioned fluid: high-speed single-molecule tracking of membrane molecules. *Annu. Rev. Biophys. Biomol. Struct.* **34**, 351–378 (2005).
53. W. L. Vaz, H. G. Kapitza, J. Stuempel, E. Sackmann, T. M. Jovin, Translational mobility of glycophorin in bilayer membranes of dimyristoylphosphatidylcholine. *Biochemistry* **20**, 1392–1396 (1981).
54. R. P. McNamara *et al*., Imaging of surface microdomains on individual extracellular vesicles in 3-d. *J. Extracell. Vesicles* **11**, e12191 (2022).
55. S. A. Gazze *et al*., High content, quantitative AFM analysis of the scalable biomechanical properties of extracellular vesicles. *Nanoscale* **13**, 6129–6141 (2021).
56. S. Li, F. Eghiaian, C. Sieben, A. Herrmann, I. A. Schaap, Bending and puncturing the influenza lipid envelope. *Biophys. J.* **100**, 637–645 (2011).
57. H. G. Lee *et al*., Nanoscale biophysical properties of small extracellular vesicles from senescent cells using atomic force microscopy, surface potential microscopy, and raman spectroscopy. *Nanoscale Horiz.* **7**, 1488–1500 (2022).
58. P. Arthur *et al*., Biophysical, molecular and proteomic profiling of human retinal organoid-derived exosomes. *Pharm. Res.* **40**, 801–816 (2023).
59. F. Stridfeldt *et al*., Analyses of single extracellular vesicles from non-small lung cancer cells to reveal effects of epidermal growth factor receptor inhibitor treatments. *Talanta* **259**, 124553 (2023).
60. M. Sun *et al*., Multiple membrane tethers probed by atomic force microscopy. *Biophys. J.* **89**, 4320–4329 (2005).
61. L. Jauffred, T. H. Callisen, L. B. Oddershede, Visco-elastic membrane tethers extracted from *Escherichia coli* by optical tweezers. *Biophys. J.* **93**, 4068–4075 (2007).
62. D. Raucher, M. P. Sheetz, Characteristics of a membrane reservoir buffering membrane tension. *Biophys. J.* **77**, 1992–2002 (1999).
63. O. P. Wiklander *et al*., Systematic methodological evaluation of a multiplex bead-based flow cytometry assay for detection of extracellular vesicle surface signatures. *Front. Immunol.* **9**, 1326 (2018).
64. R. Palmulli *et al*., CD63 sorts cholesterol into endosomes for storage and distribution via exosomes. *Nat. Cell Biol.* **26**, 1–17 (2024).
65. R. S. Gracia, N. Bezlyepkina, R. L. Knorr, R. Lipowsky, R. Dimova, Effect of cholesterol on the rigidity of saturated and unsaturated membranes: fluctuation and electrodeformation analysis of giant vesicles. *Soft Matter* **6**, 1472–1482 (2010).
66. C. Hofsäß, E. Lindahl, O. Edholm, Molecular dynamics simulations of phospholipid bilayers with cholesterol. *Biophys. J.* **84**, 2192–2206 (2003).
67. P. Rangamani, K. K. Mandadap, G. Oster, Protein-induced membrane curvature alters local membrane tension. *Biophys. J.* **107**, 751–762 (2014).
68. M. E. Hemler, Targeting of tetraspanin proteins-potential benefits and strategies. *Nat. Rev. Drug Discov.* **7**, 747–758 (2008).
69. J. P. Bost *et al*., Growth media conditions influence the secretion route and release levels of engineered extracellular vesicles. *Adv. Healthcare Mater.* **11**, 2101658 (2022).
70. X. Liang *et al*., Rapid and highly efficient mammalian cell engineering via cas9 protein transfection. *J. Biotech.* **208**, 44–53 (2015).
71. G. Corso *et al*., Reproducible and scalable purification of extracellular vesicles using combined bind-elute and size exclusion chromatography. *Sci. Rep.* **7**, 11561 (2017).
72. V. Nele *et al*., Effect of formulation method, lipid composition, and pegylation on vesicle lamellarity: A small-angle neutron scattering study. *Langmuir* **35**, 6064–6074 (2019).
73. V. V. Nguyen *et al*., Inter-laboratory multiplex bead-based surface protein profiling of MSC-derived EV preparations identifies MSC-EV surface marker signatures. *J. Extracell. Vesicles* **13**, e12463 (2024).
74. O. P. Wiklander *et al*., Systematic methodological evaluation of a multiplex bead-based flow cytometry assay for detection of extracellular vesicle surface signatures. *Front. Immunol.* **9**, 1326 (2018).
75. J. A. Welsh *et al*., Mpapass software enables stitched multiplex, multidimensional EV repertoire analysis and a standard framework for reporting bead-based assays. *Cell Rep. Methods* **2**, 100136 (2022).
76. A. Görgens *et al*., Identification of storage conditions stabilizing extracellular vesicles preparations. *J. Extracell. Vesicles* **11**, e12238 (2022).
77. A. Görgens *et al*., Optimisation of imaging flow cytometry for the analysis of single extracellular vesicles by using fluorescence-tagged vesicles as biological reference material. *J. Extracell. Vesicles* **8**, 1587567 (2019).
78. P. Parisse *et al*., Atomic force microscopy analysis of extracellular vesicles. *Eur. Biophys. J.* **46**, 813–820 (2017).
79. J. L. Hutter, J. Bechhoefer, Calibration of atomic-force microscope tips. *Rev. Sci. Instrum.* **64**, 1868–1873 (1993).
80. V. Pandey, D. Mitra, A. Dev, Atomic force microscopy (AFM) data of exosomes and liposomes. Zenodo. https://doi.org/10.5281/zenodo.15113782. Deposited 31 March 2025.